

Spontaneous oscillations in intrinsic signals reveal the structure of cerebral vasculature

Russell S. Stewart,¹ Chao Huang,^{2,4} Megan T. Arnett,² and Tansu Celikel^{3,4}

¹Undergraduate Program in Neuroscience, University of Southern California, Los Angeles, California; ²Neuroscience Graduate Program, University of Southern California, Los Angeles, California; ³Departments of Neurobiology and Biomedical Engineering, University of Southern California, Los Angeles, California; and ⁴Department of Neurophysiology, Donders Institute for Brain, Cognition and Behaviour, Radboud University Nijmegen, Nijmegen, The Netherlands

Submitted 30 December 2011; accepted in final form 25 March 2013

Stewart RS, Huang C, Arnett MT, Celikel T. Spontaneous oscillations in intrinsic signals reveal the structure of cerebral vasculature. *J Neurophysiol* 109: 3094–3104, 2013. First published April 3, 2013; doi:10.1152/jn.01200.2011.—Functional imaging of intrinsic signals allows minimally invasive spatiotemporal mapping of stimulus representations in the cortex, but representations are often corrupted by stimulus-independent spatial artifacts, especially those originating from the blood vessels. In this paper, we present novel algorithms for unsupervised identification of cerebral vascularization, allowing blind separation of stimulus representations from noise. These algorithms commonly take advantage of the temporal fluctuations in global reflectance to extract anatomic information. More specifically, the phase of low-frequency oscillations relative to global fluctuations reveals local vascular identity. Arterioles can be reconstructed using their characteristically high power in those frequencies corresponding to respiration, heartbeat, and vasomotion signals. By treating the vasculature as a dynamic flow network, we finally demonstrate that direction of blood perfusion can be quantitatively visualized. Application of these methods for removal of stimulus-independent changes in reflectance permits isolation of stimulus-evoked representations even if the representation spatially overlaps with blood vessels. The algorithms can be expanded further to extract temporal information on blood flow, monitor revascularization following a focal stroke, and distinguish arterioles from venules and parenchyma.

in vivo spectroscopy; cerebral cortex; barrel cortex; rodent; image processing

FUNCTIONAL IMAGING OF INTRINSIC signals allows quantitative analysis of neural representations by taking advantage of the coupling between vascular response and neural activity (Lieke et al. 1989; Parri and Crunelli 2003; Roy and Sherrington 1890; Sheth et al. 2005; Villringer and Dirnagl 1995). These minimally invasive hemodynamic imaging techniques commonly have low signal-to-noise ratio (SNR) and slow time course and require averaging across multiple trials to obtain reproducible results (Bonhoeffer and Grinvald 1996; Mayhew et al. 1999; Vanzetta et al. 2005; Zepeda et al. 2004; Zheng et al. 2001).

The noise in intrinsic signals exists in both spatial and temporal domains. Slow changes in wide-scale regional cerebral blood flows [rCBF (Cannestra et al. 1996; Dirnagl et al. 1989; Narayan et al. 1995; Villringer et al. 1989)], slow oscillations in the diameters of arterioles [i.e., vasomotion

(Chambers and Zweifach 1947; Kalatsky and Stryker 2003; Zepeda et al. 2004)], and higher frequency oscillations resulting from respiration and heartbeat (Lieke et al. 1989; Mayhew et al. 1996; Reidl et al. 2007) introduce temporally varying and spatially structured fluctuations to intrinsic signal measurements. Among the different sources of noise, those that closely match the time course of the vascular response to neural activity (i.e., $0.02 < f < 0.2$ Hz) have an order of magnitude larger amplitude than stimulus-evoked responses (Bonhoeffer and Grinvald 1996; Carmona et al. 1995; Zepeda et al. 2004) and have proven more difficult to overcome (Schiessl et al. 2008; Vanzetta et al. 2005) because band-pass filtering risks the loss of information from the underlying signal. This noise can be attenuated by phase-locking the stimulus onset to oscillations, subtracting the prestimulus background, and averaging evoked responses across multiple trials (Grinvald et al. 1991), which reduce the magnitude of stimulus-independent oscillations with uncorrelated phase by the square root of the number of trials (Narayan et al. 1994). Assuming greater spatial homogeneity of the slow spontaneous fluctuations in the signal, one can further reduce the noise in evoked responses by subtracting the median from each frame (Blasdel and Salama 1986; Frostig et al. 1990; Ts'o et al. 1990). This procedure corrects for the slow global changes in reflectance as a function of time (Bonhoeffer and Grinvald 1996). The combination of these approaches results in an averaged time series of hemodynamic response, which may be used to map the spatial location, amplitude, and time course of the evoked responses.

Even after these corrections, however, there often remains a spatially structured vasculature artifact that interferes with extraction of evoked representations (Spitzer et al. 2001). Early application of principal component analysis (PCA) helped to isolate the stimulus-evoked responses from stimulus-independent noise (Cannestra et al. 1996; Geladi et al. 1989; Vanzetta et al. 2004; Zheng et al. 2001) using the implicit assumption that evoked representations would be localized and elliptical and the vasculature noise would appear in branching vessel structures that are quantitatively similar to vessel maps. Although improving the quality of the mapping signal, these linear PCA methods still leave residual signals from the vasculature that confound quantitative analysis of evoked representations. This is an inevitable consequence of PCA: even the ideal time-course eigenvector of the stimulus-evoked response can produce an arteriole-corrupted spatial representation due to the physiologically coupled role of arterioles as the source of blood flow to the evoked neural response. For this reason,

Address for reprint requests and other correspondence: T. Celikel, Heyendaalseweg 135, Internal mailbox: 33, 6525 AJ Nijmegen, The Netherlands (e-mail: t.celikel@donders.ru.nl).

several variations of independent component analysis (ICA), such as extended spatial decorrelation [ESD (Molgedey and Schuster 1994; Schiessl et al. 2008; Stetter et al. 2000)], subspace correlation (Zheng et al. 2001), and spontaneous ICA [sICA (Reidl et al. 2007)], have been applied to the principal components to separate stimulus-evoked representations from spatially distinct stimulus-independent noise. Although these algorithms can successfully isolate the vasculature artifact, because they produce images with unitless dimensions and are highly non-linear by their nature, subsequent quantitative analysis of the physiological signals is often difficult (Reidl et al. 2007; Schiessl et al. 2008; Stetter et al. 2000).

For these reasons, there is a niche for approaches that would identify vasculature for isolation of stimulus-evoked representations from nonspecific changes in hemodynamic responses within the well-understood domain of reflectance units (Carmona et al. 1995; Frostig et al. 1990; Reidl et al. 2007; Schiessl et al. 2008; Stetter et al. 2000; Vanzetta et al. 2005; Zheng et al. 2001). To this end, a binary classification of the pixels that carry the largest stimulus-independent changes (i.e., lowest SNR) offers several distinct advantages. First, binary removal of pixels with a greater stimulus-independent component permits denoising without changing image units, allowing a direct extraction and quantitative interpretation of evoked representations. Second, as Carmona and colleagues (1995) originally observed, even if one does not require common units for quantitative comparison of spatial representations across trials, conditions, or experiments, initial removal of stimulus-independent artifacts before applying PCA minimizes the overlap between stimulus-evoked and stimulus-independent representations. Third, there remains an interest in the dynamics of the stimulus-evoked vasculature response (Drew et al. 2011; Golanov et al. 1994; Jones et al. 2001). Binary classification of pixels representing the vasculature may facilitate more targeted investigations into the dynamic temporal response of arterioles and venules on stimulus presentations and allow mechanistic explanation of stimulus representations using functional imaging of intrinsic signals.

Here, we introduce three novel algorithms that reconstruct vasculature pattern from temporal variations in intrinsic signals. The methods are unsupervised, allow blind source separation of the stimulus-independent noise in intrinsic signals, and are particularly suitable for automation of image processing steps for quantitative analysis of neural representations. We furthermore show that these algorithms can be expanded to

distinguish arterioles from venules, quantify the time course of blood flow in identified vasculatures, and allow reconstruction of stimulus-evoked representations even if the evoked representation spatially overlaps with vasculature.

MATERIALS AND METHODS

Adult C57BL/6 mice (22–24 g; Taconic Farms) from either sex were used according to the animal welfare guidelines of the National Institutes of Health, and experiments were approved by the Animal Care and Use Committee at the University of Southern California (protocol no. 11467).

Animal Preparation

Mice were anesthetized with ketamine and xylazine intraperitoneally (100 mg/kg ketamine, 15 mg/kg xylazine) and placed on a heating pad to maintain the core body temperature at $36.5 (\pm 0.2)^{\circ}\text{C}$ during the experiment. Following a medial skin incision, skull above the right primary somatosensory cortex was thinned to $\sim 100\text{-}\mu\text{m}$ thickness (-1.5 to -4.5 from bregma; -3 to -6 from midline) using a dental drill. Skull transparency was maintained throughout the imaging session by application of a thin layer of mineral oil (330760; Sigma-Aldrich) as necessary.

Data Acquisition

All data acquisition and instrument control were performed using custom-written routines in LabVIEW (National Instruments). Two light-guide-coupled, high-power, light-emitting diodes were used to visualize cerebral vascularization (530 nm; LCS-0530-05-22; Migh-tex) and to image intrinsic signals (625 nm; LCS-0625-03-22; Migh-tex). We chose 625-nm light for intrinsic observation because it provides a strong SNR in evoked experiments and the physiological etiology of the signal at this wavelength has been well-characterized (Frostig et al. 1990). Images were acquired at 60 frames per second using a Pike F-032B (Allied Vision Technologies) with custom thermoelectric cooling and digitized at 16 bits with 320×480 -pixel resolution. Field of view was magnified ($\times 4$; $7\text{ }\mu\text{m}/\text{pixel}$) using a custom-made macroscope (Fig. 1) attached to the camera. The camera was placed perpendicular to the imaging plane and focused $\sim 200\text{ }\mu\text{m}$ below the cortical surface. To visualize whisker-evoked changes in intrinsic signals, a single whisker (i.e., left C2) was deflected (amplitude = 8°) using a computer-controlled piezoelectric actuator every 15 s with a 5-Hz square-pulse train for 3 s. In addition, spontaneous changes in intrinsic signals were observed for a period of 5 min. All data were acquired continuously.

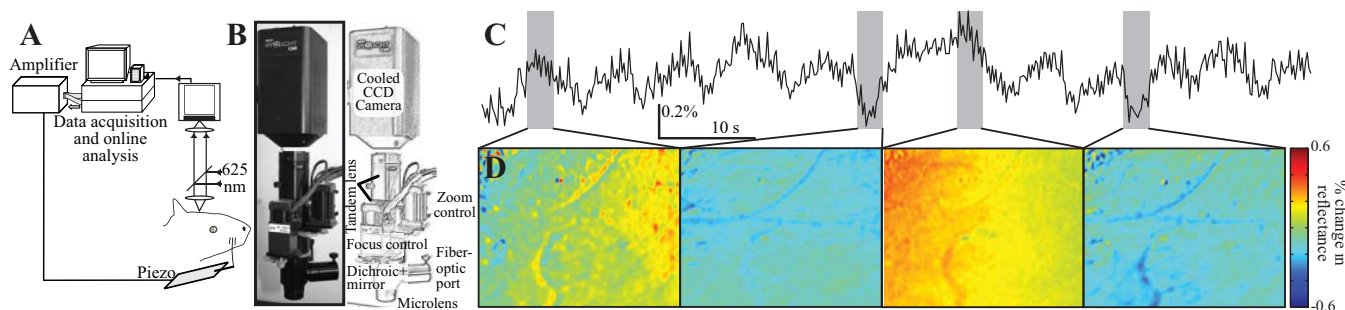


Fig. 1. Experimental setup and representative data. *A*: spontaneous and sensory-evoked changes in reflectance of 625-nm wavelength light was measured in vivo under anesthesia. Whisker deflections were delivered using a piezoelectric actuator (Piezo). CCD, charge-coupled device. *B*: custom-made macroscope for intrinsic optical imaging. *C*: spontaneous low-frequency oscillations in mean pixel reflectance over a 60-s period. *D*: representative images reconstructed from averaged reflectance over 2-s time intervals during low and high “states” of the light reflectance.

Data Analysis

Data analysis was performed using MATLAB (The MathWorks). The collection of MATLAB functions and a representative raw data set are available online as supplementary materials at the *Journal of Neurophysiology* web site. For vascular identification analyses, individual images collected under 625-nm illumination during spontaneous observation were downsampled at 8 Hz by averaging pixel values in 0.125-s frames. Background reflectance was calculated for each pixel across the period of observation (e.g., 60 s) by averaging, and percentage change in reflectance (Y) was calculated after subtraction of the background and smoothed (Y_s) using a Gaussian filter ($\sigma = 70 \mu\text{m}$). The $70\text{-}\mu\text{m}$ standard deviation of the Gaussian filter was chosen to reduce local video noise maximally with a minimal blurring effect on larger-scale image features (e.g., vessels and neural responses) and might be reduced when trying to identify smaller vessels. Sample frames of Y_s are shown in Fig. 1C (bottom). Finally, global reflectance, G , was calculated as the median value of each frame in Y_s to track spontaneous changes in intrinsic signals across the field of view (see Fig. 1C, top).

Spatial reconstruction from spectral power. Spatial reconstruction from spectral power (SRSP) is based on reconstruction of the spectral power in pixel reflectance oscillations across the field of view. This approach is feasible given the previous observations that distinct sources (i.e., heart rate, breathing, and vasomotion) that contribute to changes in intrinsic signals oscillate at different frequencies (Carmona et al. 1995; Mayhew et al. 1996; Schiessl et al. 2008; also see below). To isolate contributions of each source to changes in Y_s , we computed the Fourier power spectrum (\tilde{Y}_s). As shown in Fig. 2, the power contained in frequency peaks of \tilde{Y}_s differs for regions of interest (ROI) containing arterioles, venules, or capillaries. We use this information to construct a map of arterioles by integrating over the frequency domain (df) for each pixel (Fig. 2, B–E, bottom):

$$\text{SRSP image}(i, j) = \int_{0.2}^{4.0} \tilde{Y}_s^{i,j}(f) df. \quad (1)$$

Maximal covariance after shift. Maximal covariance after shift (MCS) is based on calculation of the phase of low-frequency fluctuations in each pixel with respect to G . Because these low-frequency

fluctuations propagate through the blood vessels, the phase of upstream arterioles leads and the phase of downstream venules lags the global phase. As a result, spatial reconstruction of phase information across the ROI correlates well with vascular classification.

For phase computation, we take advantage of the fact that two oscillating signals will have higher covariance when their respective phases are aligned. Both G and Y_s were band-pass filtered to remove frequency components >1 Hz and sphered to zero mean and unit variance, giving \hat{G} and \hat{Y}_s . By shifting the \hat{Y}_s forward or backward in time with respect to \hat{G} , we were able to modulate the phase offset and search for the phase shift that maximizes the covariance between \hat{G} and \hat{Y} . Rather than searching for the maximum over each independent shift, we increased the robustness of the phase estimation by maximizing over the quadratic regression of covariance values for shifts within a narrow window (i.e., $\in [-0.25, 0.25]$ s). After finding the phase of each pixel, we then reconstruct the field of view:

$$\text{MCS image}(i, j) = \underset{\text{shift} \in [-0.25, 0.25]}{\text{argmax}} \hat{G}(t) \cdot \hat{Y}_s^{i,j}(t + \text{shift}) \quad (2)$$

where t is time.

Local coherence with global flux. The phase differences in the vasomotion signal identified by MCS indicate that the instantaneous flow rate through each cross-section of the vascular network is not necessarily uniform. Inevitably, hemoglobin entering the field of view must travel through the arterioles before exiting through the venules. Because, during periods of increasing blood supply, the activity of the arterioles precedes that of the venules, we expected a positive correlation between the signal from arteriole vessels and the change in G and a negative correlation between the signal from venules and the change in G . As a result, we found that the sign of this correlation was indicative of vessel type. To reduce high-frequency noise, we first low-pass filter the G at 1 Hz and then calculate:

$$\text{LCGF image}(i, j) = Y_s^{i,j}(t) \cdot \partial \quad (3)$$

where LCGF is the local coherence with global flux.

Spontaneous PCA. PCA was performed on spontaneous oscillations in reflectance as described before for stimulus-evoked representations (Biswal and Kannurpatti 2009; Carmona et al. 1995; Everson

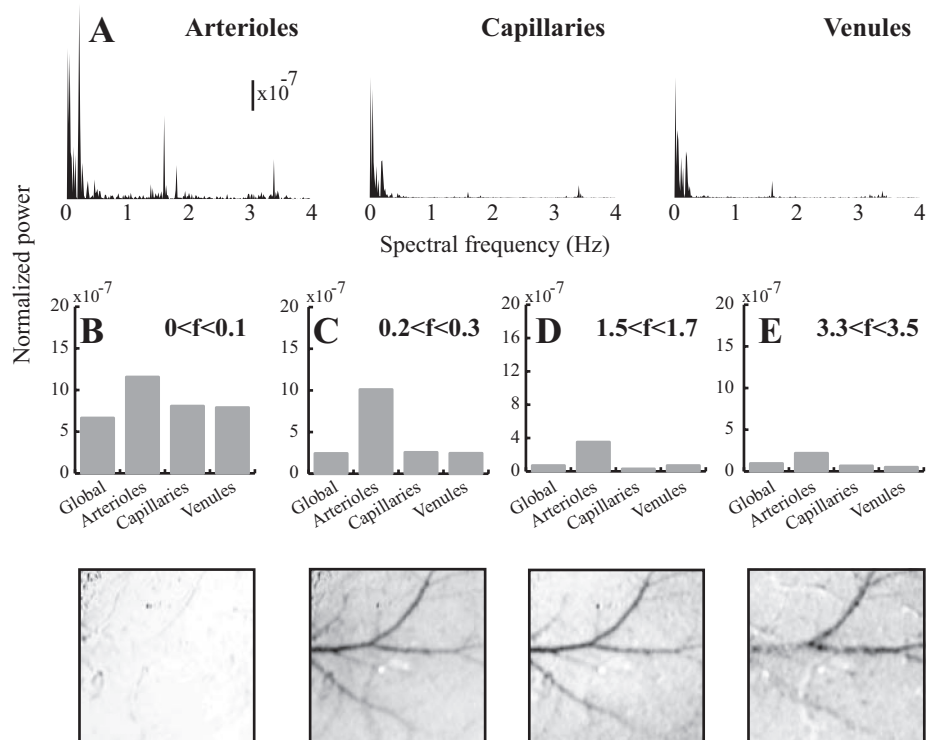


Fig. 2. Spectral power of oscillations varies across vasculatures. A: Fourier power spectrum of the mean light reflectance across frequencies for identified arterioles, capillaries, and venules. Spectral power across the entire image is shown as the change in mean pixel reflectance (i.e., global reflectance). Reconstruction of the regions of interest (ROI) from band-pass filtered data at $0 < f < 0.1$ Hz (B), $0.2 < f < 0.3$ Hz (C), $1.5 < f < 1.7$ Hz (D), and $3.3 < f < 3.5$ Hz (E). Histograms show the power in different vasculature across the same 4 Fourier spectrum peaks.

et al. 1998; Mayhew et al. 2001; Narayanan and Laubach 2009; Reidl et al. 2007; Schiessl et al. 2008; Stetter et al. 2000; Vanzetta et al. 2004; Zepeda et al. 2004) with minor modifications. Low-pass filtered ($f < 0.2$ Hz) Y_s was downsampled at 1 Hz, and continuously recorded data were segmented into 15-s long periods. The number of segments used for analysis depended on the time course and varied between 1 and 20. A composite segment, X , was formed as the average of each segment, sphered to zero mean and unit variance. The eigenvectors of the covariance matrix of X were calculated, and the principal components, shown in Fig. 3E, were generated by multiplying X by the n th eigenvector with the *Component 1* having maximal variance.

Direct visualization of vasculature under green light. A single frame of reflectance at 530 nm was used for direct visualization of the vasculature for reference purposes. To compensate for slowly varying reflectance properties, including uneven illumination, a Gaussian filter ($\sigma = 140 \mu\text{m}$) was applied. Subtraction of the smoothed image from the raw image produced a corrected image where vascularization is visualized (e.g., see Fig. 3A).

Mutual information calculations. For quantitative analysis of the success in identification of vasculature using the aforementioned algorithms, we calculated the mutual information (MI) between the vasculature as identified under 530-nm anatomic illumination (P) and each reconstruction based on functional imaging at 625 nm (Q). To calculate the MI images, P and Q were first thresholded to produce binary maps. Pixels in the highest x_P or x_Q percentiles, respectively, were assigned a value of 1, and all other pixels were assigned a value of 0. The entropy in Q was calculated as:

$$H(Q) = -f_{Q=0} \log(f_{Q=0}) - f_{Q=1} \log(f_{Q=1}). \quad (4)$$

In addition, the entropy in Q given the elements of P was calculated using the probabilities of a 0 or 1 occurring in Q given a 0 or 1 occurring in the same location of P :

$$H(Q|P) = -f_{P=0} [f_{Q=0|P=0} \log(f_{Q=0|P=0}) + f_{Q=1|P=0} \log(f_{Q=1|P=0})] - f_{P=1} [f_{Q=0|P=1} \log(f_{Q=0|P=1}) + f_{Q=1|P=1} \log(f_{Q=1|P=1})]. \quad (5)$$

From these quantities, the MI was calculated as the difference between the original entropy in Q and the entropy in Q given P :

$$\text{MI}(Q, P) = H(Q) - H(Q|P). \quad (6)$$

This calculation was repeated for a range of threshold values, $x_P \in [1:30]$ and $x_Q \in [1:30]$, producing a two-dimensional MI matrix that quantitatively compares the success of vasculature classification algorithms against a common reference image.

Analysis of sensory-evoked responses. To exemplify the use of vasculature identification algorithms for reconstruction of sensory-evoked representations, whisker deflection-evoked changes in intrinsic signals were studied as described above. Individual images collected at 60 Hz, under 625-nm illumination, were downsampled (by averaging) into 0.5-s frames for analysis. In each trial (duration: 15 s), the background reflectance was determined by averaging the last six frames before whisker deflection onset for the first-frame analysis (Frostig et al. 1990; Mayhew et al. 1996; Narayan et al. 1994; Obermayer and Blasdel 1993; Schiessl et al. 2008; Sheth et al. 2005). For each trial, the percentage change in evoked reflectance, E , was

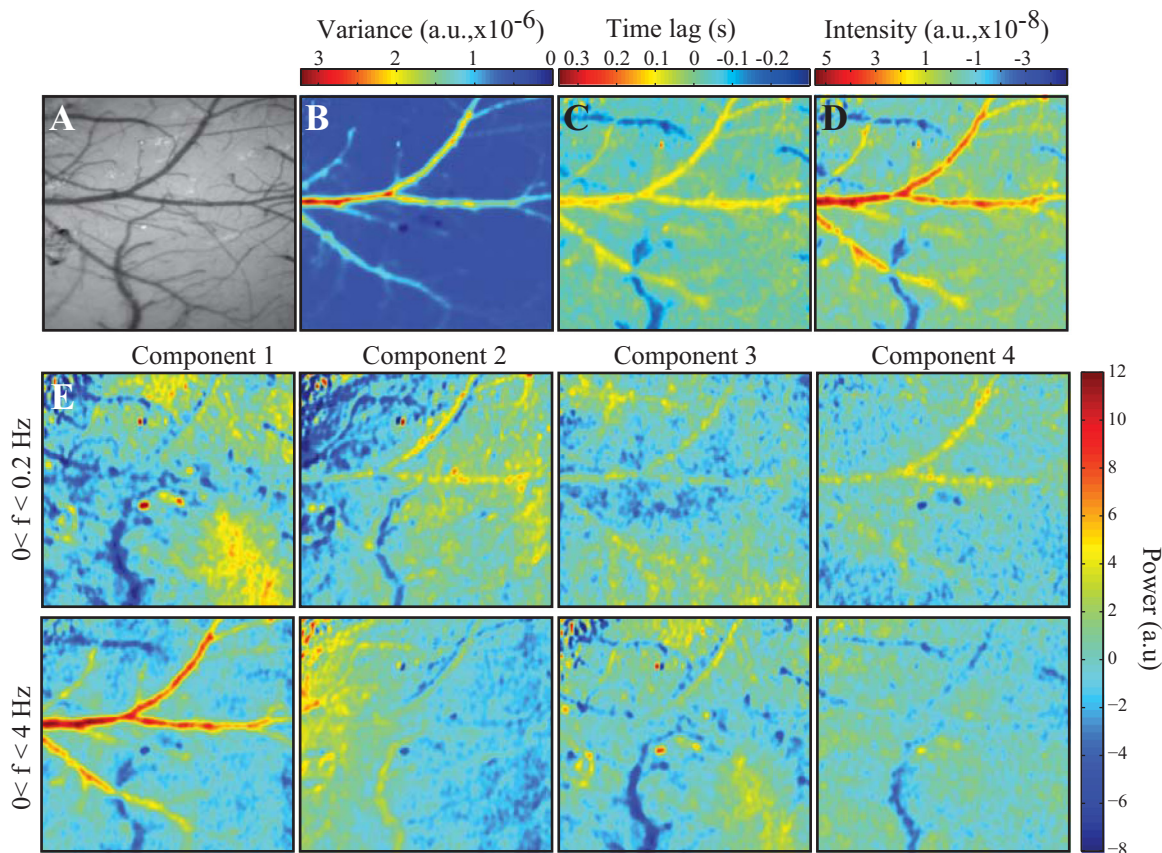


Fig. 3. Reconstruction of the cerebral vasculature from low-frequency spontaneous oscillations in light reflectance. A: cerebral vasculature visualized under 530-nm illumination, presented as reference. B: power of oscillations in $0.2 < f < 4$ Hz reconstructed into a 2-dimensional spatial representation. Note that this "Variance" method successfully detects larger arterioles with a typical branch diameter of $>35 \mu\text{m}$. C: reconstruction of the phase offset in each pixel relative to the global reflectance with maximal covariance after shift (MCS). D: reconstruction of the coherence between regional cerebral blood volume (CBV) and global cerebral blood flow (CBF) into local coherence with global flux (LCGF) image. E: 1st 4 principal components generated from low-passed (<0.2 Hz; top) and band-passed ($0 < f < 4$ Hz; bottom) percentage change in reflectance. a.u., Arbitrary units.

identified by subtracting the background image and then dividing by it. The reflectance video was then averaged across 20 trials (E_{av}) to reduce the noise in spontaneous signals not phase-locked to the stimulus.

To generate the response containing stimulus-independent pixels, E_{av} was smoothed using a Gaussian filter ($\sigma = 70 \mu\text{m}$), and the median of each frame was subtracted to reduce the effect of low-frequency noise. Figure 5D (left) shows a representative image, averaged from 1.5 to 2 s after stimulus onset.

Removal of the vasculature artifact from evoked sensory representations. To reconstruct sensory representations with reduced vasculature noise, pixels that preferentially carry stimulus-independent signal, i.e., arteriole pixels, were identified by thresholding the LCGF image (Fig. 3D; threshold: top 15%). To prevent these arteriole pixels from corrupting their surroundings during smoothing, we removed them before applying the Gaussian filter. For image smoothing after pixel removal, we developed a specialized routine. First, a binary map was created with zeros marking the identified arteriole pixels and ones marking all other pixels. Each frame of E_{av} was multiplied by the binary map, Gaussian-filtered ($\sigma = 70 \mu\text{m}$), and again multiplied by the binary map to give preadjusted frames. To correct for bias that resulted from introduction of the zero values (see above), the same Gaussian filter was applied to the binary map, resulting in an adjustment image with all values between 0 and 1. Dividing the preadjusted frames by the adjustment image (with the exclusion that $0/0 = 0$) and subtracting the median from each frame gave the final images where stimulus-independent arteriole signal is excluded. To refill the gaps denoting vasculature, each frame was bilinearly interpolated and smoothed using a Gaussian filter ($\sigma = 49 \mu\text{m}$). The final frame representing the averaged evoked response between 1.5 and 2 s after stimulus is shown in Fig. 5D (right).

RESULTS

We developed image-processing algorithms for unsupervised identification of cerebral vascularization by visualizing temporally varying fluctuations in reflectance across the field of view. One of the main applications for these algorithms is to extract stimulus-independent changes in intrinsic signals to improve quantitative analysis of sensory-evoked representations in brain-mapping experiments.

Spectral Powers of Spontaneous Oscillations Vary Across Vasculatures

To investigate the temporal characteristics of changes in light reflectance across cerebral vasculature, we plotted the \bar{Y}_s of the signal in pixels corresponding to arterioles, venules, capillaries, as well as G across the field of view (Fig. 2A). Each power spectrum is constructed from the mean value of 49 pixels in a 7×7 ROI. Spectral analysis of the global fluctuations in reflectance shows four distinct peaks at 0.05, 0.2, 1.6, and 3.4 Hz, which correspond to rate of rCBF, vasomotion, respiration, and heartbeat, respectively (Mayhew et al. 1996; Schiessl et al. 2008). The oscillatory nature of the reflectance varies across the vasculature. Whereas signals recorded in arterioles replicate the spectral signature described for G , signals from venules and capillaries oscillate predominantly in lower frequencies ($f < 0.5$ Hz; Fig. 2A).

Given the distinct spectral representation of the vasculature, image reconstruction based on band-pass filtered temporal fluctuations in intrinsic signals should reveal a pattern of vascularization. Figure 2, B–E (bottom), shows the relative success of spatial reconstructions in narrow-pass (0.1 Hz) filtered data around the frequency peaks noted above. Recon-

structions from $0 < f < 0.1$ Hz reveal little spatial dependency or vascular structure. Power in higher frequencies shows greater contrast between arterioles and other vessels or non-vessels (parenchyma; Fig. 2, C–E) with highest SNR at $0.2 < f < 0.3$ Hz. This contrast may be partially explained by vasomotion at this frequency range (Dirnagl et al. 1989; Mayhew et al. 1999; Spitzer et al. 2001).

Spatial reconstructions in the $1.5 < f < 1.6$ Hz, which correspond to rate of respiration in mouse under our anesthetic conditions, also outline arterioles, although normalized power of oscillations at this range is significantly smaller than the signal observed at $0.2 < f < 0.3$ Hz. Unlike the other peaks, the 3.4-Hz heartbeat reconstruction is not homogeneous across the arterioles. This difference suggests that pressures imposed by the microvascular structure of the arterioles might influence the signal magnitude. The heartbeat signal also contains a lower value for venules than the parenchyma (Fig. 2E) in part due to the reduced pressure of blood after flowing through the capillaries.

Transforming spectral power information into a single image. In our methods, extraction of the stimulus-independent response is achieved by classification of pixels from a single image. To produce this image, it was necessary to combine spatial reconstructions from frequencies informative of vascular structure (e.g., Fig. 2, C–E) while ignoring frequencies with a low SNR (e.g., Fig. 2B). The SRSP algorithm achieves this by linearly summing spatial reconstructions for all frequencies ≥ 0.2 Hz (Fig. 3B). The result correlates well with the arterioles identified in the snapshot at 530 nm (Fig. 3A). A linear sum over reconstructions is justified here because it intrinsically weights each frequency by its contribution to the variance of the net signal. The frequencies ≥ 0.2 Hz include information from vasomotion, heartbeat, and respiration and exclude slower changes in rCBF. Although the magnitude of slow oscillations < 0.2 Hz was not spatially informative, their phase proved to be characteristic of each structure.

Phase of Low-Frequency Oscillations Varies Across Vasculatures

Because rCBF may be considered as a physical wave, which originates in arterioles and propagates through vasculature to venules, it can be characterized by the temporal frequency of oscillations and the spatial wavelength between peaks. Empirically, we find that the wavelength of the rCBF signal is wider than the field of view such that the relative phase of any pixel at a given time uniquely determines its up- or downstream position within the fluid blood-flow network. Thus, by analyzing the typical difference between the phase of each pixel and the global phase, we can reconstruct an image representative of the vascular structure. Moreover, this information has the potential to identify and distinguish both venules and arterioles from surrounding parenchyma.

Creating a vasculature map from phase information. We applied this theory to our data set using MCS, which measures the phase offset of two signals across a range of frequencies by identifying the time shift that maximizes their covariance. We found that phase offsets between pixels, after low-pass filtering at < 1.0 Hz (Fig. 3C), correlated well with vascular identity previously determined from spectral power (Fig. 3B) and reflectance at 530 nm (Fig. 3A). In addition, unlike SRSP, MCS

classification resulted in separate labeling of arterioles, venules, and parenchyma, expanding the potential uses of spatial classification. Changes in covariance between zero shift and maximal shift were often small (mean = $1.5\text{E}-3$, max = $4.2\text{E}-2$, SD = $2.8\text{E}-3$) but highly revealing of structure (Fig. 3C).

Flow Dynamics are Representative of Vascatures

A separate motivation for measuring the spatial coherence of signals came specifically from blood flow and volume. In particular, we took advantage of the idea that changes in the total volume of blood throughout the field of view would have opposing correlations with activity in the sources (i.e., arterioles) and sinks (i.e., venules) of the network. We tested this hypothesis in our data set using the LCGF algorithm and found that the resulting map captured much of the vascular structure within the field of view (Fig. 3D).

Application of Spontaneous PCA

Unlike the SRSP, MCS, and LCGF, which attempt to identify vascular structure from distinct physiological phenomena, spontaneous PCA (sPCA) works under the principal that the vasculature will have an independent time course with greater variance than the parenchyma. It is not immediately obvious that these distinctions need be present in spontaneous observation. However, we have shown previously, using the SRSP method, that arterioles have greater power at frequencies ≥ 0.2 Hz (Fig. 2, C–E). If the corresponding variance is sufficient to justify an independent arteriole time-course eigenvector, the back-projection of that arteriole eigenvector into a spatial representation is equivalent to measuring the covariance between the signal of each pixel and the arteriole signal. In this case, the results of the MCS method predict that covariance, and therefore the spatial representation, would be strongest in the arterioles followed by the parenchyma and finally by the venules.

The sPCA algorithm used herein is based on previous implementations of PCA on evoked intrinsic signals (Carmona et al. 1995; Everson et al. 1998; Mayhew et al. 1999; Narayan et al. 1995; Reidl et al. 2007; Schiessl et al. 2008; Stetter et al. 2000; Vanzetta and Grinvald 2001; Zepeda et al. 2004), PET (Pedersen et al. 1994), and fMRI (Biswal and Kannurpatti 2009). Depending on the configuration of input parameters (e.g., period of observation, downsampling rate, and number of components), we found that the spatial representation produced in the first or second of principal component (Fig. 3E, *bottom*, Component 1) correlated with the vasculature maps obtained by MCS (Fig. 3C) and LCGF (Fig. 3D). Subsequent representations (Fig. 3E, *bottom*, Components 2–4) were dominated by signals from vasculature but did not successfully separate venules from arterioles and produced regional differences in the parenchyma.

Dependence on physiological sources. Given the success of the algorithm, we were interested in determining which frequency sources contributed to the vasculature component. We found it unlikely that heartbeat or respiration were the primary source of classification because they account for a lesser percentage of the total power (Fig. 2A) and the data were downsampled to 1 Hz during preprocessing, causing partial attenuation of frequencies during aliasing. To investigate whether vasculature was distinguished by phase offsets of

rCBFs or power distributions in vasomotion, we tested sPCA on data low-pass filtered <0.2 Hz to isolate the rCBF signal before downsampling. The results (Fig. 3E, *top*) do not show a reliable identification of vasculature. Alternatively, initial band-pass filtering $0.2 \leq f < 1.0$ Hz to isolate the vasomotion signal (results not shown) produced a vasculature component distinguishing venules from arterioles just as in the unfiltered data.

Quantitative Comparison of Vasculature Classification Methods

To compare the success of the four algorithms that reveal pattern of cerebral vascularization, we employed a MI metric that produced quantitative comparisons directly from binary maps as opposed to a metric based on analog content of the images compared (e.g., normalized covariance). As a comparator, we used the snapshot of the field of view at 530 nm (Fig. 3A).

Assumptions of MI comparison. Comparison of arteriole identification among the four 625-nm methods revealed similar performance at the optimal time course of each method (Fig. 4, A, B, D, and E). The MI between each of the binary maps produced by the SRSP, MCS, LCGF, and sPCA methods and the 530-nm snapshot are significantly above ($P < 1\text{E}-10$) the MI that would be produced by a random map, which approximately follows a χ^2 distribution with 1 degree of freedom (Federer 2011). However, interpreting the meaning of relative differences between the MI value of each method is challenging for several reasons. First, although stricter binary filters (i.e., pixels in lowest 5%) identified main arterioles for all methods, we observed that the 530-nm snapshot began filling in smaller arterioles or venules at less stringent thresholds, whereas the 625-nm methods preferentially widened main arterioles before identifying smaller vessels. This may account for the saturation in MI at 10% thresholds even though the MI between two identical images saturates at 50% thresholds. Second, the 530-nm snapshot is not an ideal classification image, and maps that have a higher MI with the snapshot are not necessarily superior. Third, the snapshot is only justified as a quantitative comparison under the assumption that all 625-nm methods will be penalized relatively equally by the intrinsic differences. It is clear that this assumption is not met for comparisons between venule and arteriole identification as both the shape and absolute maximum of MI for venule identification (Fig. 4C) were significantly different from those for arterioles. By comparison, however, the arteriole identification from vasculature maps show highly correlated shapes with the greatest correlation existing between MCS and sPCA ($r = 0.993$, $P < 0.001$ with Bonferroni correction for multiple comparisons) and the least correlation existing between SRSP and LCGF ($r = 0.953$, $P < 0.001$ with Bonferroni correction), indicating that the comparison is relatively fair.

Optimal time course of data recording. Despite these uncertainties, quantitative MI evaluation relates well to qualitative performance observations, particularly in measuring the gain or loss of information over increasing periods of observation (Fig. 4F). SRSP, MCS, and LCGF images from periods >1

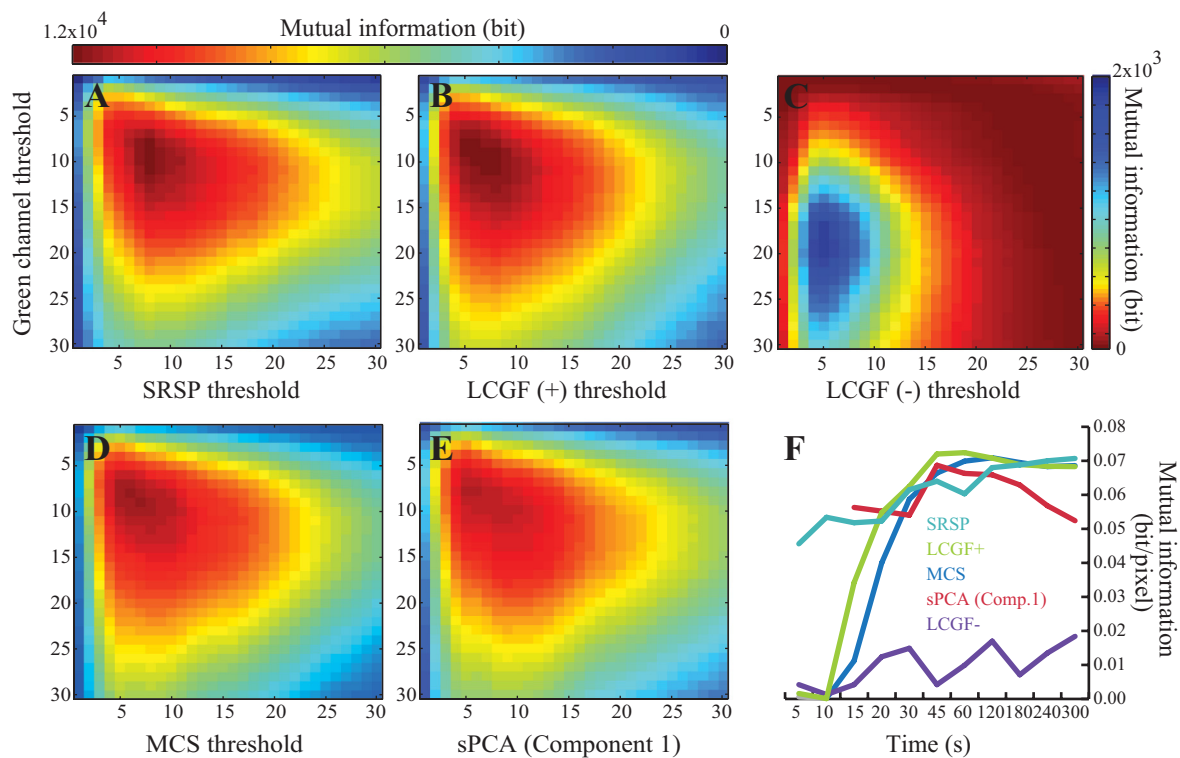


Fig. 4. Analysis of the mutual information (MI) between vasculature identified using structural imaging at 530 nm and reconstructed images from functional imaging at 625 nm using methods detailed in Fig. 3. A–E: plot of the MI between binary thresholds of the green image and reconstructions from spatial reconstruction from spectral power (SRSP) arterioles (300-s observation; A), LCGF arterioles (60-s observation; B), LCGF venules (60-s observation; C), MCS arterioles (120-s observation; D), and spontaneous principal component analysis (sPCA; Component 2, $0 < f < 4$ Hz; 45-s observation; E). Observation windows were chosen to showcase each method at its best-performing time course for arterioles. F: the relationship between MI and sampling duration. Comp. 1, Component 1.

min were computed by averaging images calculated from each minute of data before MI calculation. The information of each method is maximal at 300 s (SRSP), 120 s (MCS), 60 s (LCGF), and 45 s (sPCA).

DISCUSSION

We have introduced analytical methods for mapping cerebral vasculature using intrinsic functional optical imaging. The

algorithms are based on temporal analysis of spontaneous fluctuations in hemodynamic signals and take advantage of the spectral and phasic changes in reflectance across the vasculature. Compared with the solutions previously developed (Table 1), these algorithms allow unsupervised identification and classification of the vasculature and produce quantitatively tractable images, e.g., for blind separation of stimulus-independent changes in reflectance from evoked representations (see below).

Table 1. Comparison of published algorithms for detection and classification of vasculature

	SRSP (Fig. 3B)	MCS (Fig. 3C)	LCGF (Fig. 3D)	sPCA (Fig. 3E)	Wavelet Analysis (Carmona et al. 1995)	Evoked PCA (Cannestra et al. 1996)	ESD (Stetter et al. 2000)	sICA (Reidl et al. 2007)
Classification of vasculature into	2 Groups: arterioles; venules and parenchyma	3 Groups: arterioles; venules; parenchyma	3 Groups: arterioles; venules; parenchyma	3 Groups: arterioles; venules; parenchyma	2 Groups: arterioles and venules; parenchyma	No digital classification	No digital classification	No digital classification
Classification uses information in	Temporal domain	Temporal domain	Temporal domain	Spatial and temporal domains	Spatial and temporal domains	Spatial and temporal domains	Spatial and temporal domains	Spatial and temporal domains
Data type requirement	Evoked or spontaneous	Spontaneous	Spontaneous	Spontaneous	Evoked	Evoked	Evoked	Evoked
Units	Power	Time offset	Rate	PCA units	PCA units	PCA units	ICA units	ICA units
Requires human supervision	No	No	No	Yes	No	Yes	Yes	Yes

SRSP, spatial reconstruction from spectral power; MCS, maximal covariance after shift; LCGF, local coherence with global flux; PCA, principal component analysis; sPCA, spontaneous PCA; ESD, extended spatial decorrelation; ICA, independent component analysis; sICA, spontaneous ICA.

Principles, Underlying Assumptions, and Limitations of SRSP, MCS, and LCGF

SRSP is based on the observations (Fig. 2) that fluctuations in 625-nm reflectance are not uniform across the cortex and throughout the vasculature. The spatial dependence of power distributions may be related to the source of oscillatory changes in reflectance. For the data collected from the mouse somatosensory cortex and presented herein, discrete peaks at 0.2, 1.6, and 3.4 Hz correspond to oscillations introduced by vasomotion, respiration, and heartbeat, respectively.

Vasomotion, the spontaneous rhythmic changes in the tone of blood vessels, is closely linked to cyclic changes in CBF and cerebral blood volume (CBV) throughout the vascular network (Dirnagl et al. 1989; Mayhew et al. 1996). Given the role of arterioles in perfusion and the observation that CBF and CBV changes are largest and can be most readily studied in arterioles (Drew et al. 2011; Vanzetta et al. 2005), one would expect that arterioles would carry a dominant vasomotion signal. Our results agree with this prediction and show significantly stronger signal magnitude, at 0.2 Hz, in the arterioles rather than in venules or capillaries (Fig. 2B). Interestingly, respiration-induced changes in reflectance at 1.6 Hz show the greatest magnitude difference between the arterioles and parenchyma, providing a strong contrast for arteriole identification. The contrast between arterioles and venules, on the other hand, is maximized at 3.4 Hz, which argues that the magnitude of the heartbeat on blood flow decreases as blood circulates through capillaries. Unlike vasomotion and respiration-induced fluctuations in the intrinsic signals, heartbeat-induced oscillations show spatial inhomogeneity within the arterioles, which may be due to different pressures imposed by the microvascular structure of the arterioles.

Given the greater power in arterioles across the entire spectrum (Fig. 2), it may appear that taking the variance of each pixel would provide a reliable map of arterioles. However, we find that the greatest contribution to the variance originates from changes in regional CBF at frequencies <0.2 Hz, which show significantly less contrast between the vasculature and parenchyma than other frequency peaks. For this reason, we omit these frequencies from the final SRSP image, integrating over the power spectrum only for frequencies ≥ 0.2 Hz.

The emphasis on information from higher frequency signals for use in vessel identification may be compared with the method employed by Carmona and colleagues (1995) for wavelet analysis. Their wavelet analysis processed the raw signal by integrating over the absolute value of the time derivative of the reflectance of each pixel. When thinking of the raw signal as the sum of its sinusoidal components, the derivative weights each oscillation by its frequency, numerically penalizing the contribution from low-frequency components. Whereas Carmona and colleagues (1995) justify the derivative through physiological means, the results of our SRSP method suggest that this weighting has a direct numerical benefit by amplifying the contribution of frequencies with greater SNR.

Finally, it should be noted that our vasculature reconstruction based on SRSP would have been different, albeit only minimally, had we integrated over a log-frequency scale rather than a linear one. The decision on how to reconstruct the final SRSP image is fairly arbitrary by nature, as any method taking

linear combinations of frequency components could be justified. We chose uniformly weighted integration because of its relative simplicity, its theoretical relationship to the variance, and its success for the conditions of our experiment.

MCS algorithm is our attempt to visualize directly the phase differences between the slow oscillations in the global signal and individual pixels. Since the discovery of the slow 0.2-Hz vasomotion oscillation, its spatial coherence has been of interest (e.g., Mayhew et al. 1996). Although we have shown that the magnitude of this signal varies across different vasculature (see above), phase differences can be more difficult to visualize, as they require higher temporal resolution for detection. One method to detect phase differences between signals is to investigate the differences between the complex Fourier series of each signal. Because each physiological source of the intrinsic signals carries information across frequency range, it is necessary to combine information from more than one frequency band in the discrete Fourier spectrum. In its general form, this combination requires a metric that considers the magnitude and direction of the phase offset, the power contribution with respect to the overall signal variance, and the absolute frequency for each band of the discrete Fourier spectrum across both signals.

To accomplish this complex task, we apply the MCS algorithm, which intrinsically takes these parameters into consideration with a simple and intuitive concept: the phase of two signals will be best aligned when their covariance is maximal. If the two signals are nearly aligned to start with, as is the case for the low-frequency oscillations across the field of view, temporally shifting one signal in respect to another will act either to align better their phase, hence increasing the covariance, or to separate further the phase, decreasing the covariance. The magnitude and sign of this change depend on the initial separation, allowing computation of the offset of each pixel from the global phase across the field of view.

Our data show that the phase distribution of intrinsic signals is not random but directly associated with the flow dynamics of the network. Whereas phase of the arteriole signal leads the global phase, the phase of the venule signal follows it. Interestingly, the phase of the capillary signal is relatively well-aligned with the global phase. These observations are consistent with a model of the low-frequency oscillations propagating along arteriole-capillary-venule path of the blood flow. The difference in phase may be equated to the time required for the signal to cross the field of view, in our case ~ 0.25 s. This time window is in agreement with previous observations of the delay between CBV increase and the corresponding increase in CBF (Jones et al. 2001; Malonek et al. 1997).

LCGF. The phase differences revealed by MCS also indicate that the oscillations seen in G (Fig. 1A) are not uniform throughout the network. Moreover, the net flow through the arterioles can be greater or less than the net flow through the venules: this difference is particularly evident during evoked activity, when blood flow and oxygen levels are increased in isolated loci. When the global flow is positive, the arterioles should be carrying more blood, and the opposite should be true when the total global flow is negative. Therefore, regions with higher local CBV when the global blood volume is increasing are likely to contain arterioles, and regions with higher local CBV when global blood volume is decreasing are likely to contain venules. This relationship may be examined using

inner product of local CBV in each frame and the derivative of the global blood volume. The scalar result is positive for arterioles and negative for venules (Fig. 3D).

Spatial vs. Temporal Domain of Information in Intrinsic Signals for Vasculature Identification

Intrinsic signals are complex. Even single pixel values oscillate at various time scales, which, as we have shown, contain quantitative information regarding the cerebral vasculature. Hemodynamic signals also carry information in the spatial domain. The source of the perfusion to the neural tissue, directionality of network flow, systematic changes in the vasculature size, and functional coupling between neighboring regions all contain spatial knowledge that can be used to extract the pattern of vasculature. However, as we have shown, temporal data also contain information about the vasculature. One advantage of the temporal methods is that they are better suited for separate identification of venules and arterioles, which have otherwise similar spatial structure.

A reason for the strong performance of temporal methods is that they include the same implicit, and valuable, assumption used by spatial methods when applying a Gaussian spatial filter before temporal analysis. Although designed to decrease detector (e.g., charge-coupled device) noise, the Gaussian filter simultaneously enforces the assumption that pixels in the same region will have a similar identity. Although this assumption is well-justified by physical connectivity of blood vessels, it also causes neighboring adjacent pixels to be too similar to differentiate by further spatial analysis. As a result, most of the local spatial information is lost, placing an upper bound on the potential of continued local analysis in the spatial domain. Although spatial analysis on larger scales (e.g., distinguishing between the linear vessels and the elliptical mapping signal) remains relatively unaffected by this limitation, image-wide features are more qualitative by nature, and taking advantage of them quantitatively is both harder to justify theoretically and harder to implement algorithmically. Further spatial analysis is intrinsically penalized by the prior application of the Gaussian filter, however, the quality of information in the temporal domain is improved. This is mainly because the underlying physiological signals are spatially homogenous in local regions to begin with, and Gaussian averaging only makes their expression more robust. Essentially, this allows investigation of signals within

the frequency domain, which appears to contain independent and otherwise unexploited information.

Our methods use blind source separation, make no further assumptions about the spatial domain, and avoid tampering with image units, therefore it is possible to apply many of the powerful spatially based methods (see Introduction) on extraction of the stimulus-independent component using the frequency domain. For example, it remains to be seen whether a variation of wavelet analysis or ESD analysis could be used in combination with one or more temporal methods discussed here to enhance the current identification process.

Application of Vasculature Identification Methods in Functional Brain-Mapping Experiments

There has been a long-standing interest in vessel identification algorithms in functional imaging studies (Carmona et al. 1995; Frostig et al. 1990; Reidl et al. 2007; Schiessl et al. 2008; Stetter et al. 2000; Vanzetta et al. 2005; Zheng et al. 2001). Mapping vasculature in evoked data is particularly important as its identification will allow removal of vasculature noise from neural representations of the stimulus. Current solutions, such as subtraction of orthogonal stimulus conditions or application of PCA, ICA, sICA, ESD, and others, commonly remove vessel artifacts without reconstructing the vasculature map or identifying the type of vasculature.

As discussed previously, part of the reason these spatiotemporal algorithms struggle is that the signal in arterioles is dynamically coupled with the evoked signal. Although PCA is successful in amplifying the SNR over classic methods, it also carries some of the vessel artifacts into the mapping components (Reidl et al. 2007; Schiessl et al. 2008; Stetter et al. 2000). To clean these components, ICA may be employed to look for distinct spatial sources in the principal components. This process is designed to remove pixels in the stimulus-evoked component that also show up in the vasculature components (Reidl et al. 2007; Schiessl et al. 2008), which is essentially the same objective that our algorithms use. However, unlike binary removal methods, the penalty applied to these pixels in ICA is very hard to adjust for because it is calculated in the nonlinear domain of ICA.

We have shown that our methods are capable of producing similar results using information from the temporal domain

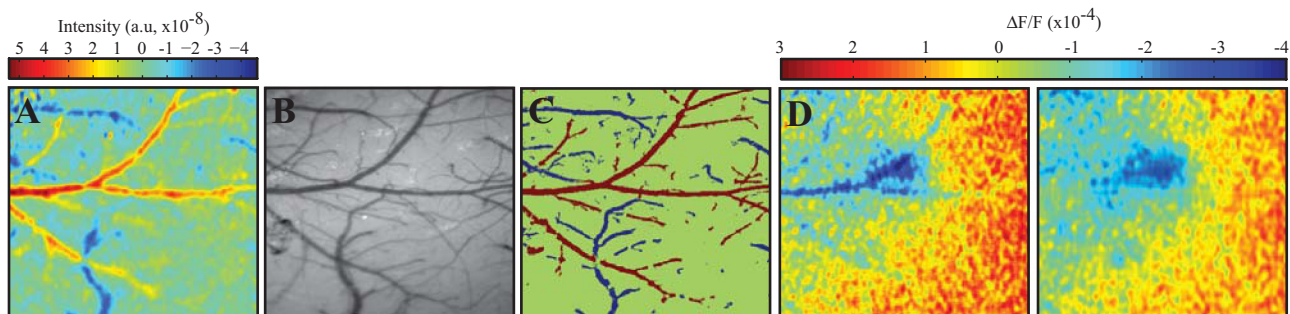


Fig. 5. Application of vasculature identification techniques for classification of blood vessels and removal of blood vessel artifacts from evoked responses. *A*: reconstruction of the coherence between local CBV and global CBF into LCGF image. *B*: raw image collected at 530 nm. *C*: back-projection of LCGF values onto vessels identified under 530 nm produces a map of arterioles (red) and venules (blue). *D*: extraction of the vasculature artifact from whisker-evoked representations in the mouse primary somatosensory cortex. *Left*: image of the percentage change in reflectance between 1.5 and 2 s after stimulus onset averaged over 20 trials shows corruption of functional response by arterioles. *Right*: whisker-evoked response after the removal of vessels identified by SRSP and recovery of removed pixels using a bilinear interpolation function.

without some of the difficulties associated with previous methods. Once vessel artifacts have been removed from the image, quantitative vessel analysis using classic methods becomes much easier, as algorithms targeted to the evoked response need not worry about the influence of noise from the vasculature.

A further advantage of removing vessels is that the subtraction of the median image after first-frame analysis (Frostig et al. 1990; Mayhew et al. 2001; Narayan et al. 1994; Obermayer and Blasdel 1993; Schiessl et al. 2008; Sheth et al. 2005) can provide a better approximation of the spontaneous noise. As seen in Fig. 2, the low-frequency noise is stronger in vessels, damaging the spatial homogeneity of the low-frequency signal. By removing vessels before the calculation of the median, the median will better represent the noise in vessel-free tissue, which is where most of the stimulus-evoked representations reside.

In addition to removing the vasculature noise, we are able to recover some of the lost information under the assumption that a removed pixel would have a similar evoked response to neighboring pixels had it not been overlapped by the vasculature. Conveniently, this assumption appears to be valid when the pixel is within the evoked response. We take advantage of this assumption by bilinearly interpolating values for removed pixels, refilling the gaps in the image (Fig. 5E).

Algorithms described herein allow direct identification and classification of the cerebral vasculature. Although they were originally developed for the blind separation of vasculature noise from evoked representations to automate quantitative analysis of sensory representations, they are likely to find other applications including measurement of phase-based flow changes to study hemodynamic coupling across large cortical territories and chronic study of revascularization following a stroke.

GRANTS

This research was supported in part by a University of Southern California Provost Fellowship (R. S. Stewart), Whitehall Foundation, and Sloan Foundation (T. Celikel).

DISCLOSURES

No conflicts of interest, financial or otherwise, are declared by the author(s).

AUTHOR CONTRIBUTIONS

R.S.S. and T.C. conceived the study, developed the algorithms, prepared the figures, and wrote the manuscript; C.H., M.T.A., and T.C. collected the data; R.S.S. performed all of the data analysis.

REFERENCES

- Biswal BB, Kannurpatti SS. Resting-state functional connectivity in animal models: modulations by exsanguination. *Methods Mol Biol* 489: 255–274, 2009.
- Blasdel GG, Salama G. Voltage-sensitive dyes reveal a modular organization in monkey striate cortex. *Nature* 321: 579–585, 1986.
- Bonhoeffer T, Grinvald A. Optical imaging based on intrinsic signals: the methodology. In: *Brain Mapping: The Methods*, edited by Toga A and Mazziotta J. San Diego, CA: Academic, 1996, p. 55–97.
- Cannestra AF, Blood AJ, Black KL, Toga AW. The evolution of optical signals in human and rodent cortex. *Neuroimage* 3: 202–208, 1996.
- Carmona RA, Hwang WL, Frostig RD. Wavelet analysis for brain-function imaging. *IEEE Trans Med Imaging* 14: 556–564, 1995.
- Chambers R, Zweifach BW. Intercellular cement and capillary permeability. *Physiol Rev* 27: 436–463, 1947.
- Dirnagl U, Kaplan B, Jacewicz M, Pulsinelli W. Continuous measurement of cerebral cortical blood flow by laser-Doppler flowmetry in a rat stroke model. *J Cereb Blood Flow Metab* 9: 589–596, 1989.
- Drew PJ, Shih AY, Kleinfeld D. Fluctuating and sensory-induced vasodynamics in rodent cortex extend arteriole capacity. *Proc Natl Acad Sci USA* 108: 8473–8478, 2011.
- Everson RM, Prashanth AK, Gabbay M, Knight BW, Sirovich L, Kaplan E. Representation of spatial frequency and orientation in the visual cortex. *Proc Natl Acad Sci USA* 95: 8334–8338, 1998.
- Federer A. *Estimating Networks Using Mutual Information* (Thesis). Zurich, Switzerland: Dept. of Mathematics, Swiss Federal Institute of Technology, 2011.
- Frostig RD, Lieke EE, Ts'o DY, Grinvald A. Cortical functional architecture and local coupling between neuronal activity and the microcirculation revealed by in vivo high-resolution optical imaging of intrinsic signals. *Proc Natl Acad Sci USA* 87: 6082–6086, 1990.
- Geladi P, Isaksson H, Lindqvist L, Wold S, Esbensen K. Principal component analysis on multivariate images. *Chemometr Intell Lab* 5: 209–220, 1989.
- Golanov EV, Yamamoto S, Reis DJ. Spontaneous waves of cerebral blood flow associated with a pattern of electrocortical activity. *Am J Physiol Regul Integr Comp Physiol* 266: R204–R214, 1994.
- Grinvald A, Frostig RD, Siegel RM, Bartfeld E. High-resolution optical imaging of functional brain architecture in the awake monkey. *Proc Natl Acad Sci USA* 88: 11559–11563, 1991.
- Jones M, Berwick J, Johnston D, Mayhew J. Concurrent optical imaging spectroscopy and laser-Doppler flowmetry: the relationship between blood flow, oxygenation, and volume in rodent barrel cortex. *Neuroimage* 13: 1002–1015, 2001.
- Kalatsky VA, Stryker MP. New paradigm for optical imaging: temporally encoded maps of intrinsic signal. *Neuron* 38: 529–545, 2003.
- Lieke EE, Frostig RD, Arieli A, Ts'o DY, Hildesheim R, Grinvald A. Optical imaging of cortical activity: real-time imaging using extrinsic dye-signals and high resolution imaging based on slow intrinsic-signals. *Annu Rev Physiol* 51: 543–559, 1989.
- Malonek D, Dirnagl U, Lindauer U, Yamada K, Kanno I, Grinvald A. Vascular imprints of neuronal activity: relationships between the dynamics of cortical blood flow, oxygenation, and volume changes following sensory stimulation. *Proc Natl Acad Sci USA* 94: 14826–14831, 1997.
- Mayhew J, Johnston D, Martindale J, Jones M, Berwick J, Zheng Y. Increased oxygen consumption following activation of brain: theoretical footnotes using spectroscopic data from barrel cortex. *Neuroimage* 13: 975–987, 2001.
- Mayhew J, Zheng Y, Hou Y, Vuksanovic B, Berwick J, Askew S, Coffey P. Spectroscopic analysis of changes in remitted illumination: the response to increased neural activity in brain. *Neuroimage* 10: 304–326, 1999.
- Mayhew JE, Askew S, Zheng Y, Porrill J, Westby GW, Redgrave P, Rector DM, Harper RM. Cerebral vasomotion: a 0.1-Hz oscillation in reflected light imaging of neural activity. *Neuroimage* 4: 183–193, 1996.
- Molgedey L, Schuster HG. Separation of a mixture of independent signals using time delayed correlations. *Phys Rev Lett* 72: 3634–3637, 1994.
- Narayan SM, Esfahani P, Blood AJ, Sikkens L, Toga AW. Functional increases in cerebral blood volume over somatosensory cortex. *J Cereb Blood Flow Metab* 15: 754–765, 1995.
- Narayan SM, Santori EM, Blood AJ, Burton JS, Toga AW. Imaging optical reflectance in rodent barrel and forelimb sensory cortex. *Neuroimage* 1: 181–190, 1994.
- Narayanan NS, Laubach M. Methods for studying functional interactions among neuronal populations. *Methods Mol Biol* 489: 135–165, 2009.
- Obermayer K, Blasdel GG. Geometry of orientation and ocular dominance columns in monkey striate cortex. *J Neurosci* 13: 4114–4129, 1993.
- Parri R, Crunelli V. An astrocyte bridge from synapse to blood flow. *Nat Neurosci* 6: 5–6, 2003.
- Pedersen F, Bergstrom M, Bengtsson E, Langstrom B. Principal component analysis of dynamic positron emission tomography images. *Eur J Nucl Med* 21: 1285–1292, 1994.
- Reidl J, Starke J, Omer DB, Grinvald A, Spors H. Independent component analysis of high-resolution imaging data identifies distinct functional domains. *Neuroimage* 34: 94–108, 2007.
- Roy CS, Sherrington CS. On the regulation of the blood-supply of the brain. *J Physiol* 11: 85–158, 1890.

- Schiessl I, Wang W, McLoughlin N. Independent components of the haemodynamic response in intrinsic optical imaging. *Neuroimage* 39: 634–646, 2008.
- Sheth SA, Nemoto M, Guiou MW, Walker MA, Toga AW. Spatiotemporal evolution of functional hemodynamic changes and their relationship to neuronal activity. *J Cereb Blood Flow Metab* 25: 830–841, 2005.
- Spitzer MW, Calford MB, Clarey JC, Pettigrew JD, Roe AW. Spontaneous and stimulus-evoked intrinsic optical signals in primary auditory cortex of the cat. *J Neurophysiol* 85: 1283–1298, 2001.
- Stetter M, Schiessl I, Otto T, Sengpiel F, Hubener M, Bonhoeffer T, Obermayer K. Principal component analysis and blind separation of sources for optical imaging of intrinsic signals. *Neuroimage* 11: 482–490, 2000.
- Ts'o DY, Frostig RD, Lieke EE, Grinvald A. Functional organization of primate visual cortex revealed by high resolution optical imaging. *Science* 249: 417–420, 1990.
- Vanzetta I, Grinvald A. Evidence and lack of evidence for the initial dip in the anesthetized rat: implications for human functional brain imaging. *Neuroimage* 13: 959–967, 2001.
- Vanzetta I, Hildesheim R, Grinvald A. Compartment-resolved imaging of activity-dependent dynamics of cortical blood volume and oximetry. *J Neurosci* 25: 2233–2244, 2005.
- Vanzetta I, Slovin H, Omer DB, Grinvald A. Columnar resolution of blood volume and oximetry functional maps in the behaving monkey; implications for fMRI. *Neuron* 42: 843–854, 2004.
- Villringer A, Dirnagl U. Coupling of brain activity and cerebral blood flow: basis of functional neuroimaging. *Cerebrovasc Brain Metab Rev* 7: 240–276, 1995.
- Villringer A, Haberl RL, Dirnagl U, Anneser F, Verst M, Einhaupl KM. Confocal laser microscopy to study microcirculation on the rat brain surface in vivo. *Brain Res* 504: 159–160, 1989.
- Zepeda A, Arias C, Sengpiel F. Optical imaging of intrinsic signals: recent developments in the methodology and its applications. *J Neurosci Methods* 136: 1–21, 2004.
- Zheng Y, Johnston D, Berwick J, Mayhew J. Signal source separation in the analysis of neural activity in brain. *Neuroimage* 13: 447–458, 2001.

